The dynamic interplay of PIP₂ and ATP in the regulation of the K$_{ATP}$ channel

Tanadet Pipatpolkai[1,2,3], Samuel G. Usher[1,3,+], Natascia Vedovato[1,+], Frances M Ashcroft[1,*], Phillip J. Stansfeld[4,*]

[1]Department of Physiology Anatomy and Genetics, Parks Road, Oxford, OX1 3PT, UK.

[2]Department of Biochemistry, South Parks Road, Oxford, OX1 3QU, UK.

[3]OXION Initiative in Ion Channels and Disease, University of Oxford, Oxford OX1 3PT, UK.

[4]School of Life Sciences & Department of Chemistry, University of Warwick, Coventry, CV4 7AL, UK.

*corresponding authors

+These authors contributed equally to the work

1

Abstract

ATP-sensitive potassium (K_{ATP}) channels couple the intracellular ATP concentration to insulin secretion. K_{ATP} channel activity is inhibited by ATP binding to the Kir6.2 tetramer and activated by phosphatidylinositol-4,5-bisphosphate (PIP_2). Here, we use molecular dynamics (MD) simulation, electrophysiology and fluorescence spectroscopy to show that ATP and PIP_2 occupy different binding pockets that share a single amino acid residue, K39. When both ligands are present, K39 shows a greater preference to co-ordinate with PIP_2 than ATP. A neonatal diabetes mutation at K39 (K39R) increases the number of hydrogen bonds formed between K39 and PIP_2, reducing ATP inhibition. We also find direct effects on nucleotide binding from mutating E179, a residue proposed to interact with PIP_2. Our work suggests PIP_2 and ATP interact allosterically to regulate K_{ATP} channel activity.

Keywords: ATP-sensitive potassium channel, molecular dynamics, phosphatidylinositol bisphosphate

Introduction

Pancreatic ATP-sensitive potassium (K_{ATP}) channels couple the energy status of the pancreatic beta-cell to insulin secretion[1]. Recent cryo-EM studies have provided high-resolution structures of the K_{ATP} channel complex, which comprises a central tetrameric pore formed from four inwardly rectifying potassium channel (Kir6.2) subunits, surrounded by four regulatory sulphonylurea receptor 1 (SUR1) subunits[2]. Binding of ATP to Kir6.2 closes the channel[3], while binding of phosphoinositides, such as phosphatidylinositol-4,5-bisphosphate (PIP_2), increases the channel open probability[4]. The ATP-binding site on Kir6.2 has been identified in several cryo-EM structures[5–10]. The PIP_2 binding site has been resolved in structural studies of related Kir channels (Kir2.2, Kir3.2)[11,12] but not yet for Kir6.2. However, its structure has been previously predicted using site-directed mutagenesis and coarse-grained molecular dynamics (CG-MD) simulation[13–15] .

Mutations in the K_{ATP} channel lead to diseases of insulin secretion. Channel hyperactivation is associated with reduced insulin secretion and neonatal diabetes mellitus (NDM) whereas reduced channel activity leads to enhanced insulin secretion and congenital hyperinsulinism (CHI)[16]. Previous studies have shown that many NDM mutations cluster at the ATP-binding site, disrupting the ATP-sensitivity of the channel[17]. Some NDM mutations also interfere with PIP_2 regulation: for example E179K enhances PIP_2 stimulation of the K_{ATP} current (as indicated by a reduction in neomycin block) and increases the predicted PIP_2 binding affinity[15,18].

The mechanism by which PIP_2 reduces ATP inhibition of the channel has long been debated. Previous studies have shown that application of PIP_2 markedly increases the channel open probability (P_{open}) and reduces channel sensitivity to ATP[19]. Because an increased channel open probability is associated with reduced ATP inhibition[20,21], it is possible that at least part of the effect of PIP_2 is mediated via changes in P_{open}. However, it has also been argued that PIP_2 may have an additional effect on ATP sensitivity that is independent of P_{open}[20]. Both molecules carry similar negatively charged phosphate groups, and previous studies have proposed that PIP_2 competes with ATP for the same binding site on the C-terminus of the protein[22]. However, comparison of recent structural studies of the channel with bound ATP[5,6], and docking and molecular dynamics simulations with PIP_2 suggest that ATP and PIP_2 have separate binding pockets[23,24].

In this study, we used atomistic molecular dynamic simulations (AT-MD) to determine the dynamics of K39 when both ATP and PIP_2 occupy their respective binding sites. These data show that K39 can co-ordinate with both ATP and PIP_2, but with stronger preference to PIP_2 when both ligands are present. We used a combination of electrophysiology and fluorescence spectroscopy to assess how mutations which affect PIP_2 binding modulate ATP inhibition and nucleotide binding. These support the simulation findings and suggest how the mutations give rise to clinical disease.

Results

In this study, we used both atomistic molecular dynamic simulations and functional studies to explore the relationship between the ATP and PIP_2 binding sites of Kir6.2.

Simulation studies: PIP_2 and ATP binding site on Kir6.2

We simulated the PIP_2 and ATP-binding sites in the Kir6.2 tetramer in the absence of SUR1 in order to exclude ATP interactions with SUR1. Previous simulations have shown there is no difference in the PIP_2 binding site when SUR1 is present[15]. Although the structure of the Kir6.2/SUR1 octameric complex has been resolved[5,6,10], there is no structure of Kir6.2 in either a PIP_2-bound or an ATP-bound conformation when SUR1 is absent. Thus, we built two atomistic simulation systems: Kir6.2 with ATP and Kir6.2 with PIP_2, and simulated each for 380 ns. To ensure that the initial protein structure was stable after converting to an atomistic system, we used pairwise root mean square deviation (RMSD) analysis over the last 300ns of the simulation on the C_α atom of Kir6.2 as a measure of the stability of protein's tertiary structure. We observed that the C_α RMSD never deviated more than 4 Å across the trajectory in all simulation set-ups. Interestingly, the simulations with bound ligand (PIP_2 or ATP) showed slightly less C_α rearrangement than the apo state. This suggests that the 3D structure of the protein is highly stable throughout our simulation, and maybe further stabilised by the ligand (Figure 1, Supplementary figure 1). To investigate the effect of PIP_2 and ATP binding at their binding sites, we select amino acid residues that were within 4 Å of the ligand for >40% of the time and defined them as contacting residues. We found that in the last 300 ns of the simulation, the contacts made with the ligands were in good agreement with previous electrophysiological and computational studies (Figure 1A,1B)[13,14].

In the PIP_2 binding site, we found that R54 and K67 from one subunit, and R176 from an adjacent subunit co-ordinate with the 4' phosphate of PIP_2, and that K39 co-ordinates with the 5' phosphate. Other uncharged residues (W68 and P69) that lie at the membrane-water interface also make strong contact with PIP_2. With the exception of P69, mutations at these residues have previously been shown to alter channel ATP sensitivity, increase the open probability and/or alter PIP_2 activation[24–27]. By evaluating the root mean square fluctuation (RMSF) of all contact residues, we found that the binding of PIP_2 statistically reduces the dynamics of the K67 and R176 side chains (Supplementary figure 2A). However, only the difference at K67 showed biological significance (defined as a decrease of ~1 Å or more).

These results agree well with previous coarse-grained simulations and hence, validate the co-ordination geometry of PIP_2 in its binding site.[13,15].

In the ATP binding site, we found that R50 co-ordinates with both the β and the γ phosphate, K39 co-ordinates with the γ phosphate and K185 co-ordinates with the α and the β phosphate (Figure 1B). Both R50 and K185 dynamics were stabilised when ATP binds to the channel (Supplementary figure 2B). These findings agree with previous studies in which the ATP-binding residues in Kir6.2 were mapped using site-directed mutagenesis [28,29]. Interestingly, the sidechain of K39 which is *ca.* 7 Å from the ATP molecule in the cryo-EM structure moves towards ATP and makes a contact in some simulations. All residues that contact ATP in the cryo-EM structure of the octameric Kir6.2/SUR1 complex (N48, I49, Q52, I182, F183, L205, Y330, S331, F333) also make contact in our simulations. These residues have been found to be crucial for ATP inhibition in functional studies [28]. Mutations in residues that make contact with ATP also cause neonatal diabetes [17].

The competition between PIP_2 and ATP for K39 co-ordination

Previous studies have shown that PIP_2 reduces channel ATP inhibition[4,19,30,31]. However, it was not clear if PIP_2 competes directly for the ATP binding site or if it interferes with ATP-dependent gating (or both). Comparison of the cryo-EM structure of the ATP binding site with the predicted PIP_2 binding site suggest they lie *ca.* 25 Å from one another[5,15]. In our studies, K39 contacts both ATP and PIP_2 in independent simulations, but the position of the amine head group is different. We next explored the dynamics of K39 when both ligands occupied their respective binding sites (Figure 2A). We calculated the distance between ATP or PIP_2 and the amine group of K39. We observed that the position of the amine head group of K39 oscillated between co-ordination with ATP and PIP_2, but favoured PIP_2 more strongly (Figure 2B and Supplementary figure 3). Interestingly, a significant decrease (P = 0.001) in ATP contact only occurred at residue K39 when PIP_2 was present (Figure 2C). Thus, we hypothesise that K39 may change its co-ordination from ATP to PIP_2 when both molecules are bound. Interestingly, the contact between K39 and PIP_2 remained unchanged in both in the presence and the absence of ATP (Figure 2D). Thus, we propose that the salt bridges between K39 and ATP are broken in the presence of the PIP_2, causing the amine group on K39 to swing towards the PIP_2 headgroup.

With the exception of K39, no other residues in either the ATP or PIP_2 binding site changed their contact probabilities, when both ligands were simultaneously present in their respective binding sites.

Neonatal diabetes mutation (K39R)

A mutation at K39 (K39R) is associated with transient neonatal diabetes[32]. This mutation does not alter the charge (as both lysine and arginine are positively charged), but an amine is replaced with a guanidium group. This would likely increase the channel affinity to both PIP_2 and ATP. We simulated Kir6.2 containing the K39R substitution and compared the contacts between the guanidium group of the arginine and PIP_2 or ATP. In simulations with ATP alone, residue 39 in the mutant channel (arginine) spent more time in contact with ATP than that (lysine) of the wild-type channel (Supplementary figure 4). In simulations with PIP_2 alone, residue 39 in both wild-type and mutant channels spent almost all of its time co-ordinated with PIP_2, but the 95% confidence interval was small for the mutant channel. When both ATP and PIP_2 were present, we found that the contact probability of residue 39 with the PIP_2 headgroup was not significantly different in the either absence or the presence of the ATP (Figure 3A, 3B). From this, we conclude that K39R mutation does not affect channel preference for PIP_2 in either the presence or the absence of ATP.

To quantify the strength of the interaction between PIP_2 and K39 or K39R, we carried out a hydrogen bond (H-bond) analysis to determine the number of H-bonds formed between the PIP_2 headgroup and the side chain of residue 39. Note that arginine can form up to 5 H-bonds spread over 3 amine groups, whereas lysine is only able to form a maximum of 3 bonds from a single amine. We observed that the guanidium group on the arginine forms two hydrogen bonds with the PIP_2 headgroup, whereas the lysine amine group forms only a single hydrogen bond. In both cases, the hydrogen bonds were formed with the 5' phosphate on the PIP_2 inositol headgroup both in the presence and the absence of the ATP (Figure 3C, 3D). This suggests that the K39R mutation enhances the strength of the interaction of residue 39 with PIP_2. We postulate this leads to reduced channel inhibition by ATP, and thereby impairs insulin secretion leading to neonatal diabetes.

Electrophysiology and Fluorescence Spectroscopy

We next used functional studies to determine if the predicted change in PIP_2 binding associated with the K39R mutation affects the ATP sensitivity of the K_{ATP} channel and if this is mediated by changes in ATP binding.

There are two distinct hypotheses for how PIP_2 binding to Kir6.2 affects nucleotide binding to Kir6.2. These are non-exclusive and both may occur simultaneously. The first (theory A)

postulates that PIP_2 binding preferentially stabilises the open state of the channel, increasing the open probability (P_{open}) and antagonising ATP inhibition indirectly. This theory predicts that ATP binding *per se* will be unaffected but this has not been measured directly. However, it has previously been shown that PIP_2 increases P_{open}[4,30] and that an increase in P_{open} reduces ATP inhibition of the K_{ATP} channel[20,21]. The second (theory B) is that PIP_2 binding to the channel antagonises ATP binding directly: this could be described as a local allosteric effect. In the case of K39, our simulations are consistent with theory B, as K39 appears to coordinate both ATP and PIP_2, and therefore binding of one necessarily will have a local allosteric effect on binding of the other.

To test this hypothesis, we examined the functional effect of mutations at K39 in two ways; by measuring the ability of ATP to inhibit the K_{ATP} current and by exploring ATP binding using a FRET-based assay with fluorescent trinitrophenyl (TNP)-ATP as a congener for ATP[33,34]. The latter method utilises FRET between channels labelled with the fluorescent unnatural amino acid 3-(6-acetylnaphthalen-2-ylamino)-2-aminopropanoic acid (ANAP) at residue W311 of Kir6.2 and TNP-ATP. Incorporation of ANAP into Kir6.2 was achieved as described previously[33–36]. A GFP tag was also added at the C-terminus of Kir6.2 to facilitate identification of transfected cells. HEK293T cells were transfected with control or mutant Kir6.2 and wild-type SUR1 and currents measured in inside-out membrane patches. All constructs described in this section have GFP at the C-terminus and are co-expressed with SUR1 (unless otherwise stated) to increase surface membrane trafficking[37]. Experiments were carried out in the absence of Mg^{2+}, to prevent Mg-nucleotide modulation of channel activity by SUR1. Constructs labelled with ANAP at residue W311 are denoted as Kir6.2*.

A reduction in K_{ATP} channel inhibition by ATP may be mediated by an increase in the unliganded P_{open}, by a decrease in ATP binding, and/or by modifying the transduction process by which ATP occupancy of its binding site is translated into altered gating. Because K39 forms part of both PIP_2 and ATP binding pockets, we also examined a residue (E179) that is predicted to form part of the PIP_2 binding site but which does not contact ATP in the cryo-EM structure[5–7,9,10,13,15]. We might therefore expect that any effect on ATP binding and inhibition caused by E179 mutations would be mediated indirectly, either via changes in P_{open} or by allosteric effects on binding.

Reduction in K_{ATP} current inhibition by ATP and TNP-ATP

We first examined the effect of mutations at K39 and E179 on ATP inhibition. We introduced three different residues at K39 (K39A, K39E, K39R) and two different residues at E179

(E179A, E179K). When these mutations were introduced into Kir6.2, we observed a statistically significant reduction in current inhibition by ATP (i.e. an increase in the IC_{50}) for each mutation tested, with the exception of K39A, which was indistinguishable from the control construct (Supplementary figure 5 and Supplementary table 1). Labelling the nucleotide binding site of Kir6.2 with ANAP (Kir6.2*) caused a reduction in ATP inhibition (from an IC_{50} of 34 μM to 112 μM). However, all mutations that caused a significant decrease in ATP inhibition in the Kir6.2 background still caused a significant decrease when in the Kir6.2* background (Figure 4A-D, and Supplementary table 2).

As the simulations were conducted with Kir6.2 in the absence of SUR1, we also examined ATP inhibition when mutant Kir6.2 was expressed alone (Supplementary table 3). We observed low current amplitudes for all constructs except Kir6.2-K39A, for which we were unable to resolve any current. The IC_{50} values for each construct were dramatically increased (by roughly an order of magnitude) when compared to the values measured when co-expressed with SUR1. Importantly, the mutant channels remained less sensitive to ATP than controls. We also transfected mutant Kir6.2* alone, but were unable to resolve any macroscopic currents. Thus, we focused our experiments on Kir6.2/SUR1 constructs.

Because measurement of ATP binding requires the use of fluorescent TNP-ATP, we next measured the effects of the five mutations introduced into Kir6.2 on TNP-ATP inhibition of the channel (Figure 5A-D). TNP-ATP is a more potent inhibitor of the K_{ATP} channel than ATP [33,34], reducing the IC_{50} from 34 μM to 1.4 μM (Supplementary table 4). Four of the five mutations (K39A, K39E, E179A, E179K) displayed a similar reduction in current inhibition when tested with TNP-ATP to that found for ATP (Figure 5G, Supplementary table 4).

Finally, we simultaneously measured current inhibition and nucleotide binding by TNP-ATP in the Kir6.2* background using patch-clamp fluorometry (Figure 5E,F,H and Supplementary table 5,6). Both E179A and E179K mutations resulted in a significant reduction in current inhibition (from an IC_{50} of 7μM for Kir6.2* to 28 μM and 169 μM for Kir6.2*-E179A and Kir6.2*-E179K respectively) and TNP-ATP binding (from an EC_{50} of 94 μM to 170 μM and 171 μM for Kir6.2*-E179A and Kir6.2*-E179K respectively). However, despite observing a significant reduction in TNP-ATP binding to Kir6.2*-K39R (from an EC_{50} of 94 μM to 209 μM), we did not find a significant decrease in current inhibition.

We fit our combined TNP-ATP binding and inhibition data to an allosteric model of K_{ATP} described previously[33,34]. This model seeks to describe channel gating with three parameters: L is a measure of the unliganded channel open probability, which in part reflects PIP_2

regulation, K_A is the binding affinity for nucleotides, and D is the global allosteric constant which represents the degree to which nucleotide binding favours the closed state of the channel. We estimated posterior probability distributions for these parameters for each mutation (Supplementary figure 6A-B) using a Bayesian Markov chain Monte Carlo (MCMC) method[38]. We observed very broad posterior probabilities for L, which we believe reflects a range of observed open probabilities, likely due to differences in channel rundown or variability in membrane PIP$_2$ between patches. However, this does not affect our estimates of the other two parameters D and K_A [33].

Our parameter estimates for Kir6.2*-E179A and Kir6.2*-E179K channels suggest that the observed reduction in current inhibition by nucleotides is mostly due to a reduction in their ability to bind, as represented by decreases in the posterior probability distributions for K_A (Supplementary figure 6C). The E179K mutation also leads to a modest increase in D, implying that transduction between the ATP binding site and gating is weakened by the mutation. Each of the mutations at K39 leads to a reduction in K_A, with the magnitude of the shift increasing R<E<A. In addition, K39E leads to a similar increase in D to that observed for E179K.

Discussion

Our work provides a mechanistic explanation for how PIP$_2$ and ATP binding influence one another to modulate the K_{ATP} channel activity. We show that in addition to its effects on P$_{open}$ [4,19,30], PIP$_2$ modulates ATP binding via long distance (E179) and local (K39) interactions.

The PIP$_2$ binding site is conserved across Kir channel structures[11,12] and previous simulation studies have suggested that residue E179 forms part of the PIP$_2$ binding site of Kir6.2[13,15]. Mutation of E179 reduces neomycin sensitivity of K_{ATP} currents supporting a role for this residue in PIP$_2$ binding[15]. Although E179 does not lie within the ATP-binding site[5,6,9,10], the E179A and E179K mutations cause a significant decrease in current inhibition by ATP or TNP-ATP, both for the control Kir6.2 construct and for that labelled with ANAP. Binding of TNP-ATP was also significantly decreased by the E179A and E179K mutations. This is consistent with the idea that mutations at E179 influence ATP binding via changes in PIP$_2$ binding or changes in P$_{open}$. Analysis of these data using our MWC model indicates this cannot be due to a change in unliganded P$_{open}$ alone, or solely due to a change in transduction, but rather due to a clear decrease in the microscopic K_A. While this might be caused by a direct influence of the mutation at the ATP-binding pocket, this would not be consistent with the existing cryo-

EM structures[5–7,9,10]. Thus, our data suggest that in the case of the E179 mutations, TNP-ATP binding is affected allosterically. Coupled with previous simulations showing that the E179K mutation enhances PIP_2 binding[15]. We suggest that this allosteric effect may be mediated by a change in PIP_2 binding.

Our atomistic MD simulations suggest that a single key residue, K39, forms part of both the ATP and PIP_2 binding sites. When both ligands are present, K39 has a stronger preference for co-ordination with PIP_2 than with ATP. This reduces the channel affinity for the ATP as K39 is no longer available to co-ordinate the ATP γ phosphate (Figure 6A-C). No other residue (in either site) alters its contact probability in the presence of the other ligand. The simulation data are supported by our finding that mutation of lysine 39 to arginine (K39R) led to a significant decrease in current inhibition by ATP. A similar reduction was found for K39E but not for K39A. However, a reduction in ATP sensitivity has been previously reported for the K39A mutation[26,39]. Introducing an ANAP label into Kir6.2 reduced ATP inhibition for control (K39) channels and even more for mutant (K39E/R/A) channels. Unfortunately, the effect of K39 mutations on TNP-ATP inhibition did not replicate the effects seen for ATP or in our simulations. In particular, there was no longer a significant difference in TNP-ATP inhibition when K39 was mutated to arginine. This may be due to the location of K39 in the ATP binding site – there is potentially a steric clash between the side chain of residue 39 and the TNP moiety of TNP-ATP (Supplementary figure 7). Although we saw shifts in the EC_{50} for fluorescence quenching, and associated shifts in the estimated microscopic association constant (K_A) for TNP-ATP, it is difficult to interpret these shifts meaningfully. This is because differences in TNP-ATP binding may not accurately reflect differences in ATP binding for the K39 mutant channels.

Nevertheless, the effects of the K39R mutation on current inhibition by ATP, together with our simulations, lead us to propose a mechanism for how the K39R mutation may cause transient neonatal diabetes. We found that the mutation increases the number of H-bonds between the side chain of residue 39 and the PIP_2 headgroup (Figure 6D). This enhances PIP_2 affinity, which in turn reduces the ability of ATP to close the channel and causes a reduction in insulin secretion that leads to neonatal diabetes.

In summary, our work is consistent with PIP_2 regulating the function of Kir6.2 both by enhancing the P_{open} of the channel, and by allosterically modulating the binding of ATP. In addition, we have demonstrated a mechanism by which mutations at residue 39 can lead to neonatal diabetes. They do so by enhancing PIP_2 binding which leads to a reduced sensitivity of Kir6.2 to ATP inhibition.

11

Materials and methods

Coarse-Grained system preparation

The human Kir6.2 model without SUR1 (PDB entry: 6BAA)[5] was converted to a coarse-grained model using *martinize.py*, embedded in the palmitoyl oleoyl phosphatidylcholine (POPC) bilayer and solvated in water and 0.15M NaCl using a self-assembly MEMPROTMD pipeline[40]. All simulations were carried out in MARTINI2.2 biomolecular forcefield[41]. The tertiary and quaternary structures of the protein were maintained through the application of an elastic network with a force constant of 1,000 kJ/mol/nm^2 between two coarse-grained backbone particles within 0.5-0.9 nm. A temperature of 323 K was maintained with V-rescale temperature coupling[42], while 1 atm pressure was controlled using semi-isotropic Parrinello-Rahman pressure coupling[43]. The position of the coarse-grained PIP_2 is taken from the chicken Kir2.2-PIP_2:diC8[11] after conversion to a coarse grain model[44]. Systems were energy minimised using the steepest descents algorithm and equilibrated for 1 μs. All simulations were carried out using GROMACS-2019.4[45].

Atomistic simulation set up

The coarse-grained simulation system (Kir6.2, lipids - PIP_2 and POPC, ions and water) was converted to atomistic using the CG2AT pipeline[46]. The K39R mutant model was generated using PyMOL with the minimum initial stearic clashes[47]. The exact position of the ATP molecule was taken from the cryo-EM structure (PDB entry: 6BAA) and placed in the Kir6.2 ATP binding site. The initial position of the hydrogen atoms was added using PyMOL. All simulations were carried out using CHARMM36 biomolecular forcefield with the virtual sites on the proteins and lipids CH_3 and NH_3^+ groups[48,49], allowing the integration timestep of 4 fs in the production run. The force field for the ATP molecule was derived from the CHARMM-GUI[50,51]. In this study, 4 different conditions were set (Apo, ATP-bound, PIP_2-bound, both ATP and PIP_2 bound) and simulations were carried out for 3 repeats.

The systems were energy minimised using the steepest descents algorithm with non-hydrogen atoms restrained at 1000 kJ/mol/nm^2. This was then followed by a 5 ns equilibration for the system where the C_α backbone on the protein and the non-hydrogen atoms on the ATP molecules were restrained with 1000 kJ/mol/nm^2 with 4 fs timesteps. A temperature of 310 K was maintained with V-rescale temperature coupling, while 1 atm pressure was controlled using semi-isotropic Parrinello-Rahman pressure coupling[43]. The simulation was then further equilibrated with only C_α restraint on the protein for another 15 ns in similar conditions. Then a 380ns production run was implemented, in which the first 80 ns of the simulations were discarded as equilibration. All simulations, H-bond calculations and distance calculation were

calculated using GROMACS-2019.4[45]. We used MDAnalysis to calculate pairwise RMSD to define change in protein dynamics across the trajectory[52–55]. As Kir6.2 is a symmetrical homo-tetramer, we assume that all sites behave identically under a short simulation timescale (380 ns). Thus, the results from our calculations are obtained over all 4 monomeric sites, making a total of 12 data points for all calculations.

Molecular biology

Human Kir6.2 and SUR1 were subcloned into pCGFP_EU (GFP-tagged constructs) and pcDNA4/TO, respectively. Site-directed mutagenesis and amber stop codons were introduced using the QuikChange XL system (Stratagene; San Diego, CA), and verified by sequencing (DNA Sequencing and Services; Dundee, Scotland), as previously described[33]. HEK-293T cells were grown in in Dulbecco's Modified Eagle Medium (DMEM, Sigma) with the addition of 10% fetal bovine serum, 100 U/mL penicillin, and 100 µg/mL streptomycin (Thermo Fisher Scientific; Waltham, MA) at 37°C, 5%/95% CO_2/air. Cells were seeded in T25 flasks 24 hours, before transfection with TransIT-LT1 (Mirus Bio LLC; Madison, WI). Transfected cells were incubated at 33 °C, 5%/95% CO_2/air. Protein expression and trafficking to the plasma membrane were optimized by including 300 µM tolbutamide in the transfection media (Yan et al., 2007; Lin et al., 2015). ANAP-tagged Kir6.2 constructs were cultured in the presence of 20 µM ANAP (free acid, AsisChem; Waltham, MA) and 48 hours post-transfection, cells were re-plated onto either poly-D-lysine coated glass-bottomed FluoroDishes (FD35-PDL-100, World Precision Instruments) or poly-L-lysine coated 35 mm petri dishes (Corning). pCDNA4/TO and pANAP were obtained from Addgene. peRF1-E55D (*Homo sapiens*) and pCGFP_EU (*Aequorea victoria*) were kind gifts from the Chin Laboratory (MRC Laboratory of Molecular Biology, Cambridge UK) and Gouaux Laboratory (Vollum Institute, Portland OR USA), respectively.

Electrophysiology

Extracellular (pipette) solutions contained (in mM) 140 KCl, 1 EGTA, 10 HEPES (pH 7.3 with KOH). The intracellular (bath) solutions contained (in mM) 140 KCl, 1 EDTA, 1 EGTA, 10 HEPES (pH 7.3 with KOH). Inside-out patches were excised from transfected HEK cells using borosilicate glass pipettes (GC150F-15, Harvard Apparatus; Holliston, MA) pulled to a resistance of 1-3 MΩ. Data were acquired at a holding potential of -60 mV using an Axopatch 200B amplifier and a Digidata 1322A digitizer run through pClamp 9 software (Molecular Devices; San Jose, CA). Currents were low-pass filtered at 1-5 kHz and digitized at 10-20 kHz.

Patches were perfused with an 8-channel μFlow or a manual gravity perfusion system. Different concentrations of adenosine triphosphate (ATP, Sigma) or fluorescent trinitrophenyl adenosine triphosphate (TNP-ATP, Jena Bioscience) were added to the bath solution to assess current inhibition and/or nucleotide binding. Nucleotide-induced inhibition was corrected for rundown by alternating test concentrations of nucleotide solution with nucleotide-free solution. The inhibition was expressed as a fraction of the control currents before and after the test solution as described previously[56]. For experiments with TNP-ATP, the zero current level was determined by perfusing 10 mM $BaCl_2$ at the end of each recording at a holding potential of +60 mV. Current inhibition data were fitted with the following Hill equation:

$$\frac{I}{I_{max}} = 1 - I_{max} + \frac{I_{max}}{1 + 10^{(IC_{50} - [nucleotide]) \cdot -h}}$$

Fluorescence measurements

Fluorescence spectra from excised patches were collected and analysed as described previously[33]. Briefly, the tip of the patch pipette was centred on the slit of the spectrometer immediately after patch excision. ANAP was excited using a 385 nm LED source (ThorLabs; Newton, NJ) with a 390/18 nm band-pass excitation filter, after which the emitted light passed through a 400 nm long-pass emission filter (ThorLabs) and an IsoPlane 160 Spectrometer (Princeton Instruments; Trenton, NJ) with a 300 grooves mm^{-1} grating. Images were collected with 1 s exposures on a Pixis 400BR_eXcelon CCD (Princeton Instruments). Spectra were corrected for background fluorescence, then ANAP intensity was calculated by averaging the fluorescence intensity measured between 469.5 nm and 474.5 nm. This intensity was corrected for bleaching with a single exponential decay. Fluorescence quenching data were fitted with the following Hill equation:

$$\frac{F}{F_{max}} = \frac{1}{1 + 10^{(EC_{50} - [TNP-ATP]) \cdot -h}}$$

Statistics and data presentation

Concentration-response data are plotted as the mean response at each tested concentration, with error bars representing the 95% confidence interval around the mean calculated from a normal distribution. IC_{50} and EC_{50} values obtained from patch-clamp and patch-clamp fluorometry experiments with TNP-ATP and ATP were compared with a one-way ANOVA, and differences between mutations at K39 and E179 to the control constructs were tested for significance with Dunnett's post-hoc test.

Monod-Wyman-Changeaux model fitting

14

The MWC-type model fitted here is described by the following sets of equations:

$$\frac{F}{F_{max}}$$

$$= \frac{K_A[TNP-ATP] \cdot (1 + K_A[TNP-ATP])^3 + LDK_A[TNP-ATP] \cdot (1 + DK_A[TNP-ATP])^3}{(1 + K_A[TNP-ATP])^4 + L(1 + DK_A[TNP-ATP])^4}$$

$$\frac{I}{I_{max}} = \frac{L(1 + DK_A[TNP-ATP])^4}{(1 + K_A[TNP-ATP])^4 + L(1 + DK_A[TNP-ATP])^4} \cdot \frac{1 + L}{L}$$

The full rationale behind this model choice is laid out in Puljung *et al* (2019). In this model, *L* represents an equilibrium constant where the K_{ATP} open probability (P_{open}) is equal to *L/(L+1)*, reflecting the ability of K_{ATP} to open and close in the absence of nucleotides. Each ligand binding event (*K_A*) is independent and each bound ligand favours the closed state by the same factor (*D*). This model is fit to the combined current inhibition and fluorescence quenching data using the brms (Bayesian Regression Models using 'Stan') package[57] in R. Prior probability distributions were supplied for each parameter as follows:

$$log_{10}(L) \sim Normal(\mu : 0, \sigma^2 : 0.7)$$
$$log_{10}(K_A) \sim Uniform(min : 2, max : 6)$$
$$D \sim Uniform(min : 0, max : 1)$$

The model was run with tetrameric Kir6.2 and ATP (and /or PIP_2) present in all 4 subunits for 4,000 iterations including a burn-in period of 2,000 iterations for a total of 8,000 samples. Each model parameter achieved a minimum effective sample size of 5,000 and a potential scale reduction statistic (R̂) of 1.00.

Acknowledgements

Author contributions

T.P. performed the coarse-grained and atomistic molecular dynamics simulations. N.V. and S.U. performed the molecular biology, electrophysiology and fluorescence measurements. All authors jointly designed the experiments, analysed the data and wrote the manuscript.

Competing interests

The authors declare no competing interests.

Funding

References

1. Rorsman, P. & Ashcroft, F. M. Pancreatic β-Cell Electrical Activity and Insulin Secretion: Of Mice and Men. *Physiol. Rev.* (2018). doi:10.1152/physrev.00008.2017

2. Puljung, M. C. Cryo-electron microscopy structures and progress toward a dynamic understanding of K_{ATP} channels. *J. Gen. Physiol.* (2018). doi:10.1085/jgp.201711978

3. Tucker, S. J., Gribble, F. M., Zhao, C., Trapp, S. & Ashcroft, F. M. Truncation of Kir6.2 produces ATP-sensitive K^+ channels in the absence of the sulphonylurea receptor. *Nature* **387**, 179–183 (1997).

4. Baukrowitz, T. *et al.* PIP$_2$ and PIP as determinants for ATP inhibition of KA$_{TP}$ channels. *Science (80-.).* **282**, 1141–1144 (1998).

5. Martin, G. M., Kandasamy, B., DiMaio, F., Yoshioka, C. & Shyng, S.-L. Anti-diabetic drug binding site in a mammalian KATP channel revealed by Cryo-EM. *Elife* **6**, e31054 (2017).

6. Lee, K. P. K., Chen, J. & Mackinnon, R. Molecular structure of human katp in complex with ATP and ADP. *Elife* **6**, (2017).

7. Wu, J.-X. *et al.* Ligand binding and conformational changes of SUR1 subunit in pancreatic ATP-sensitive potassium channels. *Protein Cell* **9**, 553–567 (2018).

8. Ding, D., Wang, M., Wu, J.-X., Kang, Y. & Chen, L. The Structural Basis for the Binding of Repaglinide to the Pancreatic K_{ATP} Channel. *Cell Rep.* **27**, 1848-1857.e4 (2019).

9. Martin, G. M. *et al.* Mechanism of pharmacochaperoning in a mammalian KATP channel revealed by cryo-EM. *Elife* **8**, e46417 (2019).

10. Li, N. *et al.* Structure of a Pancreatic ATP-Sensitive Potassium Channel. *Cell* **168**, 101-110.e10 (2017).

11. Hansen, S. B., Tao, X. & MacKinnon, R. Structural basis of PIP2 activation of the classical inward rectifier K+ channel Kir2.2. *Nature* **477**, 495–498 (2011).

12. Whorton, M. R. & MacKinnon, R. Crystal structure of the mammalian GIRK2 K+ channel and gating regulation by G proteins, PIP$_2$, and sodium. *Cell* **477**, 199–208 (2011).

13. Stansfeld, P. J., Hopkinson, R., Ashcroft, F. M. & Sansom, M. S. P. PIP2-binding site in Kir channels: Definition by multiscale biomolecular simulations. *Biochemistry* **48**, 10926–10933 (2009).

14. Shyng, S. L., Cukras, C. A., Harwood, J. & Nichols, C. G. Structural determinants of PIP(2) regulation of inward rectifier K(ATP) channels. *J. Gen. Physiol.* **116**, 599–608 (2000).

15. Pipatpolkai, T., Corey, R. A., Proks, P., Ashcroft, F. M. & Stansfeld, P. J. Evaluating

18

inositol phospholipid interactions with inward rectifier potassium channels and characterising their role in disease. *Commun. Chem.* **3**, 147 (2020).

16. Ashcroft, F. M. ATP-sensitive potassium channelopathies: Focus on insulin secretion. *Journal of Clinical Investigation* **115**, 2047–2058 (2005).

17. Pipatpolkai, T., Usher, S. G., Stansfeld, P. J. & Ashcroft, F. M. KATP channel mutations and neonatal diabetes — structural mechanisms and therapy. *Nat Rev Endocrinol* (2020).

18. De Franco, E. *et al.* Update of variants identified in the pancreatic β-cell K$_{ATP}$ channel genes KCNJ11 and ABCC8 in individuals with congenital hyperinsulinism and diabetes. *Hum. Mutat.* **41**, 884–905 (2020).

19. Fan, Z. & Makielski, J. C. Phosphoinositides decrease ATP sensitivity of the cardiac ATP-sensitive K(+) channel. A molecular probe for the mechanism of ATP-sensitive inhibition. *J. Gen. Physiol.* **114**, 251–269 (1999).

20. Enkvetchakul, D., Loussouarn, G., Makhina, E., Shyng, S. L. & Nichols, C. G. The kinetic and physical basis of K(ATP) channel gating: toward a unified molecular understanding. *Biophys. J.* **78**, 2334–2348 (2000).

21. Trapp, S., Proks, P., Tucker, S. J. & Ashcroft, F. M. Molecular Analysis of ATP-sensitive K Channel Gating and Implications for Channel Inhibition by ATP. *J. Gen. Physiol.* **112**, 333 LP – 349 (1998).

22. MacGregor, G. G. *et al.* Nucleotides and phospholipids compete for binding to the C terminus of K$_{ATP}$ channels. *Proc. Natl. Acad. Sci.* **99**, 2726 LP – 2731 (2002).

23. Haider, S., Antcliff, J. F., Proks, P., Sansom, M. S. P. & Ashcroft, F. M. Focus on Kir6.2: A key component of the ATP-sensitive potassium channel. *Journal of Molecular and Cellular Cardiology* **38**, 927–936 (2005).

24. Haider, S., Tarasov, A. I., Craig, T. J., Sansom, M. S. P. & Ashcroft, F. M. Identification of the PIP$_2$-binding site on Kir6.2 by molecular modelling and functional analysis. *EMBO J.* **26**, 3749–3759 (2007).

25. Männikkö, R. *et al.* A conserved tryptophan at the membrane-water interface acts as a gatekeeper for Kir6.2/SUR1 channels and causes neonatal diabetes when mutated. *J. Physiol.* **589**, 3071–3083 (2011).

26. Cukras, C. A., Jeliazkova, I. & Nichols, C. G. The role of NH$_2$-terminal positive charges in the activity of inward rectifier K$_{ATP}$ channels. *J. Gen. Physiol.* **120**, 437–446 (2002).

27. Shyng, S.-L., Cukras, C. A., Harwood, J. & Nichols, C. G. Structural Determinants of PIP$_2$ Regulation of Inward Rectifier K$_{ATP}$ Channels. *J. Gen. Physiol.* **116**, 599 LP – 608 (2000).

28. Tucker, S. J. *et al.* Molecular determinants of KATP channel inhibition by ATP. *EMBO*

19

J. **17**, 3290–3296 (1998).

29. Dabrowski, M., Tarasov, A. & Ashcroft, F. M. Mapping the architecture of the ATP-binding site of the K_{ATP} channel subunit Kir6.2. *J. Physiol.* **557**, 347–354 (2004).

30. Shyng, S. L. & Nichols, C. G. Membrane phospholipid control of nucleotide sensitivity of K_{ATP} channels. *Science (80-.).* **282**, 1138–1141 (1998).

31. Hilgemann, D. W. & Ball, R. Regulation of Cardiac Na^+/Ca^{2+} Exchange and K_{ATP} Potassium Channels by PIP_2 *Science (80).* **273**, 956 LP – 959 (1996).

32. Zhang, M. *et al.* Sulfonylurea in the treatment of neonatal diabetes mellitus children with heterogeneous genetic backgrounds. *J. Pediatr. Endocrinol. Metab.* **28**, 877–884 (2015).

33. Usher, S. G., Ashcroft, F. M. & Puljung, M. C. Nucleotide inhibition of the pancreatic ATP-sensitive K+ channel explored with patch-clamp fluorometry. *Elife* **9**, e52775 (2020).

34. Puljung, M., Vedovato, N., Usher, S. & Ashcroft, F. Activation mechanism of ATP-sensitive K^+ channels explored with real-time nucleotide binding. *Elife* **8**, e41103 (2019).

35. Chatterjee, A., Guo, J., Lee, H. S. & Schultz, P. G. A Genetically Encoded Fluorescent Probe in Mammalian Cells. *J. Am. Chem. Soc.* **135**, 12540–12543 (2013).

36. Zagotta, W. N., Gordon, M. T., Senning, E. N., Munari, M. A. & Gordon, S. E. Measuring distances between TRPV1 and the plasma membrane using a noncanonical amino acid and transition metal ion FRET. *J. Gen. Physiol.* (2016). doi:10.1085/jgp.201511531

37. Zerangue, N., Schwappach, B., Jan, Y. N. & Jan, L. Y. A New ER Trafficking Signal Regulates the Subunit Stoichiometry of Plasma Membrane K_{ATP} Channels. *Neuron* **22**, 537–548 (1999).

38. Hines, K. E., Middendorf, T. R. & Aldrich, R. W. Determination of parameter identifiability in nonlinear biophysical models: A Bayesian approach. *J. Gen. Physiol.* **143**, 401–416 (2014).

39. Tucker, S. J. *et al.* Molecular determinants of K(ATP) channel inhibition by ATP. *EMBO J.* **17**, 3290–3296 (1998).

40. Stansfeld, P. J. *et al.* MemProtMD: Automated Insertion of Membrane Protein Structures into Explicit Lipid Membranes. *Structure* **23**, 1350–1361 (2015).

41. Marrink, S. J., Risselada, H. J., Yefimov, S., Tieleman, D. P. & de Vries, A. H. The MARTINI Force Field: Coarse Grained Model for Biomolecular Simulations. *J. Phys. Chem. B* **111**, 7812–7824 (2007).

42. Bussi, G., Donadio, D. & Parrinello, M. Canonical sampling through velocity rescaling.

J. Chem. Phys. **126**, 14101 (2007).

43. Parrinello, M. & Rahman, A. Polymorphic transitions in single crystals: A new molecular dynamics method. *J. Appl. Phys.* **52**, 7182–7190 (1981).

44. de Jong, D. H. *et al.* Improved Parameters for the Martini Coarse-Grained Protein Force Field. *J. Chem. Theory Comput.* **9**, 687–697 (2013).

45. Abraham, M. J. *et al.* Gromacs: High performance molecular simulations through multi-level parallelism from laptops to supercomputers. *SoftwareX* **1–2**, 19–25 (2015).

46. Stansfeld, P. J. & Sansom, M. S. P. From coarse grained to atomistic: A serial multiscale approach to membrane protein simulations. *J. Chem. Theory Comput.* **7**, 1157–1166 (2011).

47. Schrodinger LLC. The PyMOL Molecular Graphics System, Version 1.8. (2015).

48. Olesen, K., Awasthi, N., Bruhn, D. S., Pezeshkian, W. & Khandelia, H. Faster Simulations with a 5 fs Time Step for Lipids in the CHARMM Force Field. *J. Chem. Theory Comput.* (2018). doi:10.1021/acs.jctc.8b00267

49. Huang, J. & Mackerell, A. D. CHARMM36 all-atom additive protein force field: Validation based on comparison to NMR data. *J. Comput. Chem.* **34**, 2135–2145 (2013).

50. Kim, S. *et al.* CHARMM-GUI ligand reader and modeler for CHARMM force field generation of small molecules. *J. Comput. Chem.* **38**, 1879–1886 (2017).

51. Jo, S., Kim, T., Iyer, V. G. & Im, W. CHARMM-GUI: A web-based graphical user interface for CHARMM. *J. Comput. Chem.* **29**, 1859–1865 (2008).

52. Beckstein, O., Denning, E. J., Perilla, J. R. & Woolf, T. B. Zipping and Unzipping of Adenylate Kinase: Atomistic Insights into the Ensemble of Open↔Closed Transitions. *J. Mol. Biol.* **394**, 160–176 (2009).

53. Gowers, R. J. *et al.* MDAnalysis: A Python Package for the Rapid Analysis of Molecular Dynamics Simulations. *Proc. 15th Python Sci. Conf.* 98–105 (2016).

54. Michaud-Agrawal, N., Denning, E. J., Woolf, T. B. & Beckstein, O. MDAnalysis: A toolkit for the analysis of molecular dynamics simulations. *J. Comput. Chem.* **32**, 2319–2327 (2011).

55. Theobald, D. L. Rapid calculation of RMSDs using a quaternion-based characteristic polynomial. *Acta Crystallogr. Sect. A* **61**, 478–480 (2005).

56. Proks, P., de Wet, H. & Ashcroft, F. M. Activation of the K_{ATP} channel by Mg-nucleotide interaction with SUR1. *J. Gen. Physiol.* **136**, 389–405 (2010).

57. Bürkner, P.-C. brms: An R Package for Bayesian Multilevel Models Using Stan. *J. Stat. Software, Artic.* **80**, 1–28 (2017).
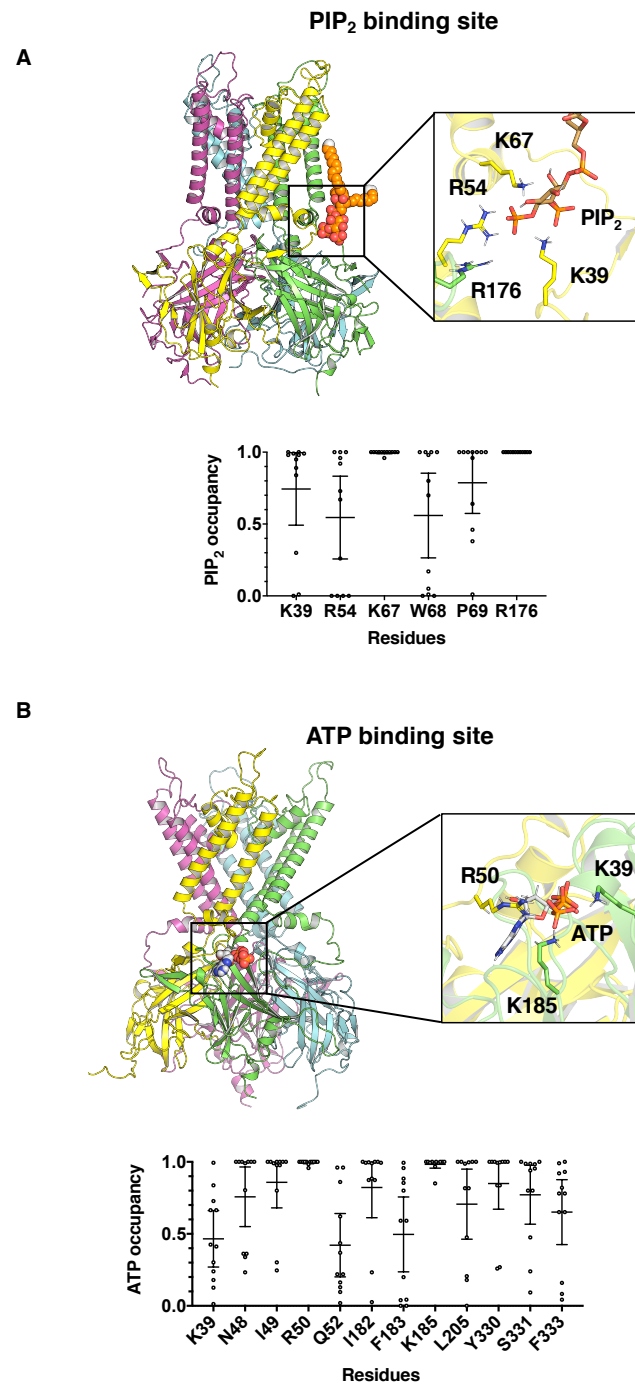
Figure 1. ATP and PIP₂ binding sites. A) Above, structure of Kir6.2 tetramer with bound PIP₂. Inset Interactions between PIP₂ (bronze) and basic residues in two chains of Kir6.2 (yellow and green). Below, fraction of time that residues which contact the PIP₂ headgroup >40% of the time in 4 subunits of three 300 ns simulations (a total of n = 12) lie in 4 Å proximity to the channel (PIP₂ occupancy). The error bar indicates the 95% confidence interval around the mean. B) Above, Structure of Kir6.2 tetramer with bound ATP. Inset, interactions between ATP (CPK) and basic residues in two chains of Kir6.2 (yellow and green). Below, fraction of time that residues which contact ATP >40% of the time in all 4 subunits of three 300 ns simulations (a total of n = 12) lie in 4 Å proximity to the channel (ATP occupancy). The error bar indicates the 95% confidence interval around the mean.
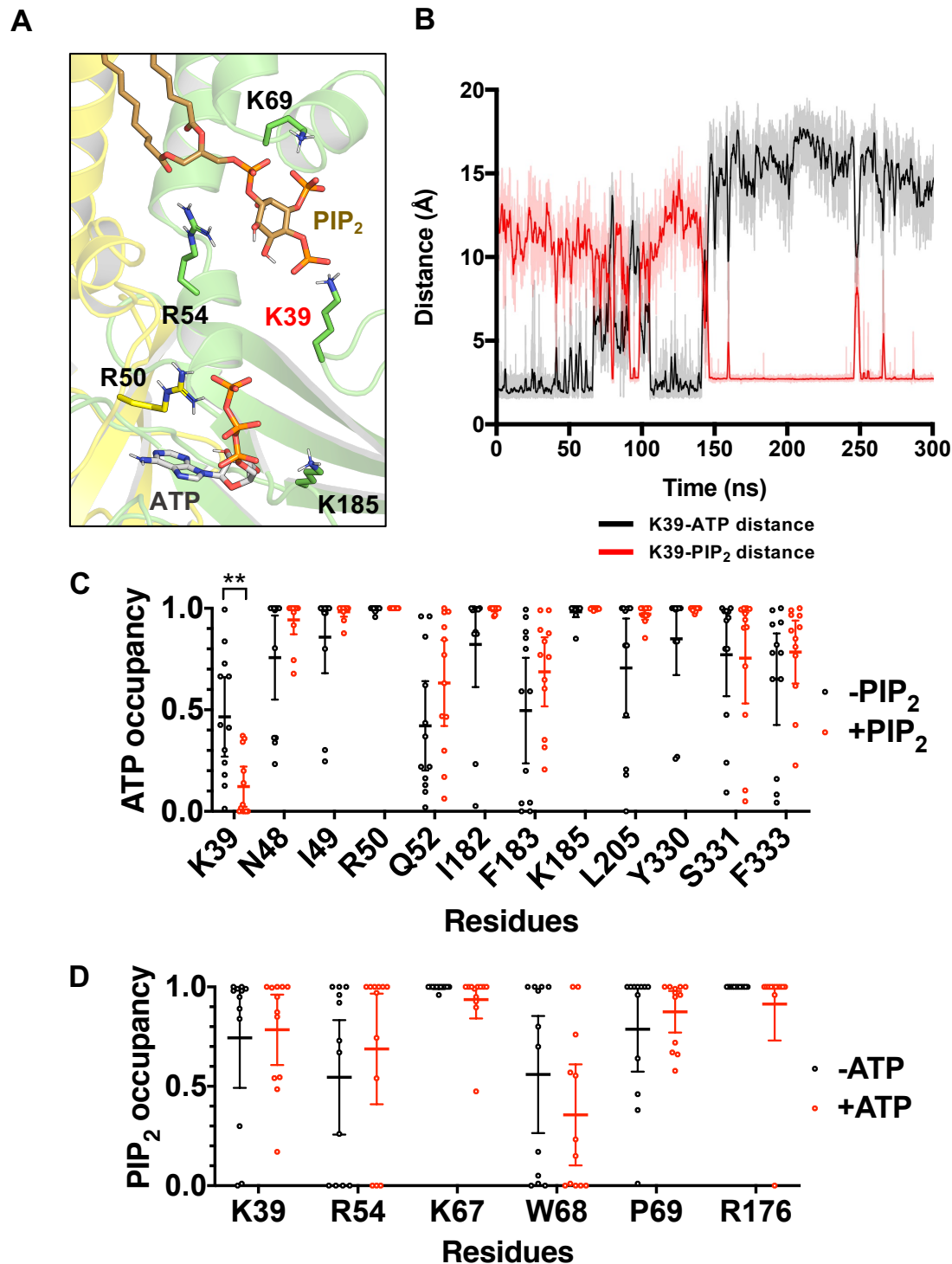
Figure 2. Changes in the ATP and PIP$_2$ binding sites when both ligands are present. A) Interactions between Kir6.2 (two subunits are indicated in yellow and green), ATP (CPK) and the PIP$_2$ (bronze) headgroup. Only the basic residues of the protein are shown. B) A representative trace showing the distance calculation between K39 and ATP (black) and K39 and PIP$_2$ (red) across a single 300ns trajectory. The darker lines show running averages of every 1 ns of the simulation. C) ATP contact analysis showing the fraction of time that residues which contact the ATP molecule >40% in all 12 repeats of 300 ns simulations are in 4 Å proximity to the channel (ATP occupancy) in the absence (black) and presence (red) of PIP$_2$. The error bar indicates the 95% confidence interval around the mean. ** p< 0.01 using Student's t-test. D) PIP$_2$ contact analysis showing the fraction of time that residues which contact the PIP$_2$ molecule >40% in all 12 repeats of 300 ns simulations are in 4 Å proximity to the channel (PIP$_2$ occupancy) in the absence (black) and presence (red) of ATP. The error bar indicates the 95% confidence interval around the mean.
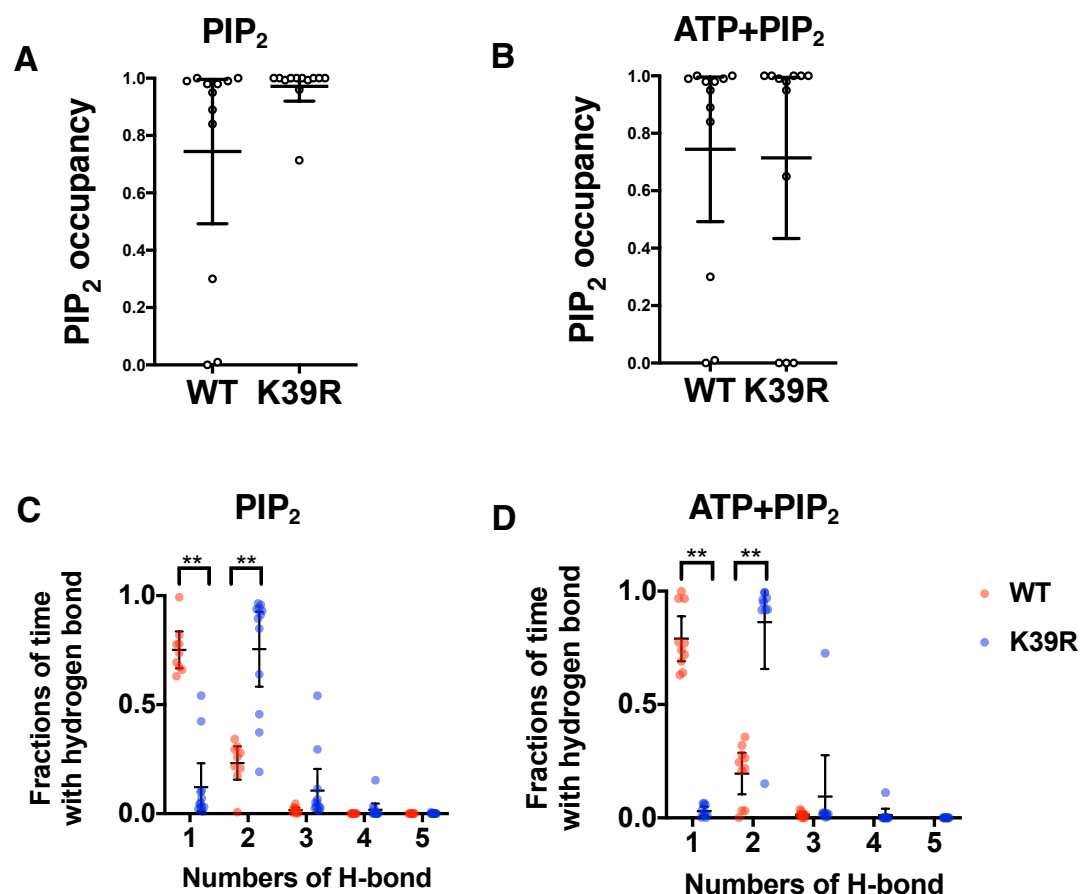
Figure 3

Figure 3. The K39R mutation changes the PIP$_2$ binding configuration. A, B) PIP$_2$ contact analysis showing the fraction of time that K39 (or K39R) is within 4 Å proximity to PIP$_2$ across all four subunits in three 300 ns simulations (a total of n = 12). The error bar indicates the 95% confidence interval around the mean in (A) the absence of PIP$_2$ or (B) the presence of PIP$_2$. C) Hydrogen bond analysis showing the fraction of time when K39 (red) or K39R (blue) forms a different number of H-bonds with the PIP$_2$ headgroup in 4 subunits of three 300 ns simulations (a total of n = 12), when only PIP$_2$ is present. The error bar indicates the 95% confidence interval around the mean. ** $p < 0.01$ (Student's t-test). D) Hydrogen bond analysis showing the fraction of time when K39 (red) or K39R (blue) forms different numbers of H-bond with the PIP$_2$ headgroup in 4 subunits of three 300 ns simulations (a total of n = 12) when both ATP and PIP$_2$ are present. The error bar indicates the 95% confidence interval around the mean. ** $p < 0.01$ (Student's t-test).
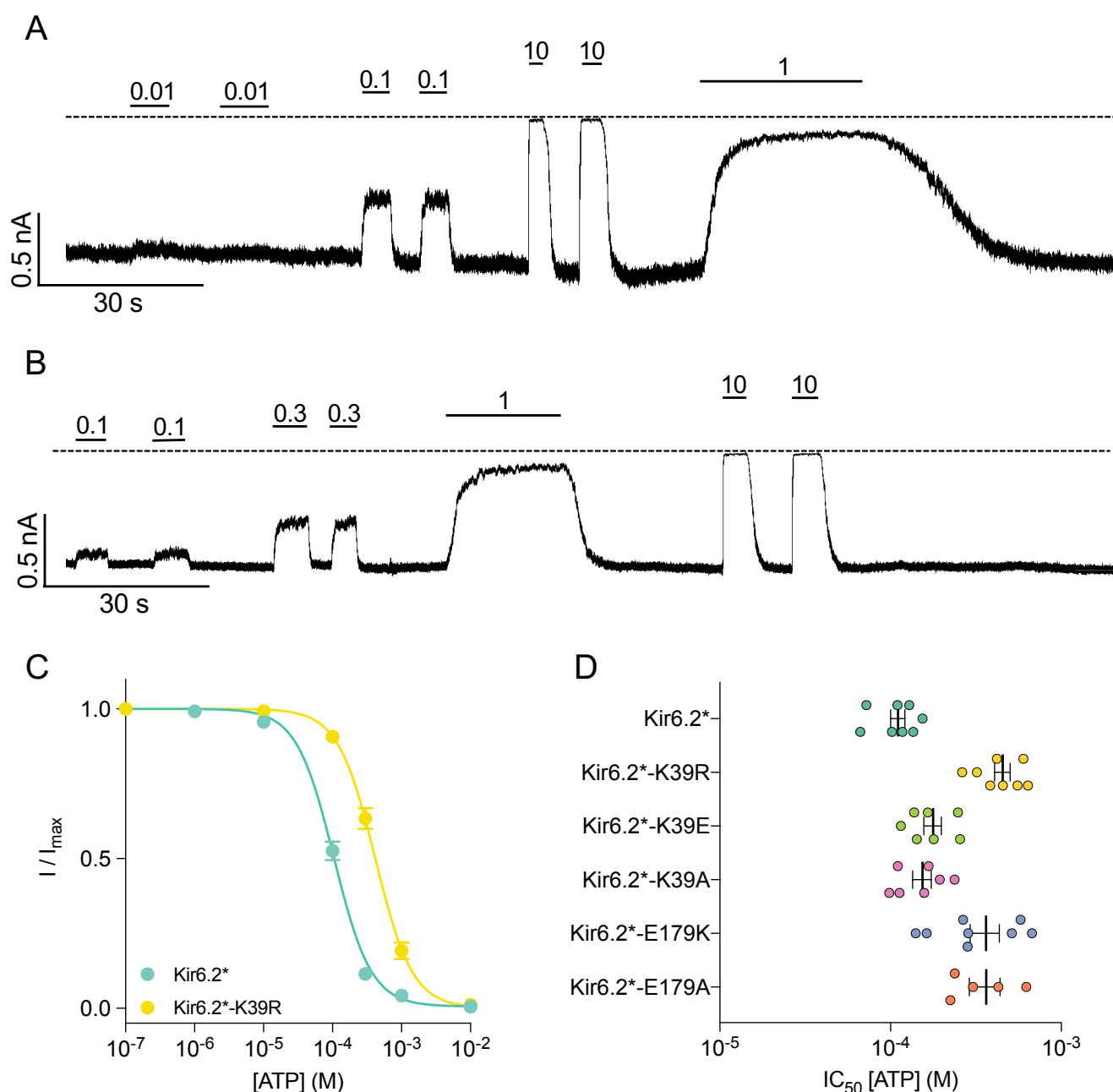
Figure 4

Figure 4. Effect of ATP on K_{ATP} current. A, B) Representative traces for Kir6.2* (A), and Kir6.2*-K39R (B). Top solid bars mark the different ATP concentrations applied (in mM). Dashed line indicates the zero-current level. B) Concentration-response relationships for ATP inhibition of Kir6.2* and Kir6.2*-K39R currents (I/I_{max}), fitted to the Hill equation. IC_{50}: 105 µM for Kir6.2*, 417 µM for Kir6.2*-K39R, fitted with common, but free, h=1.6 amd I_{max} fixed to 1. C) IC_{50}s from ATP current inhibition derived from Hill fits to individual experiments are plotted as coloured data points. The means and 95% confidence intervals for each construct are overlaid as black error bars. Each construct is labelled with GFP at the C-terminus, with ANAP at residue W311, and is co-expressed with SUR1.
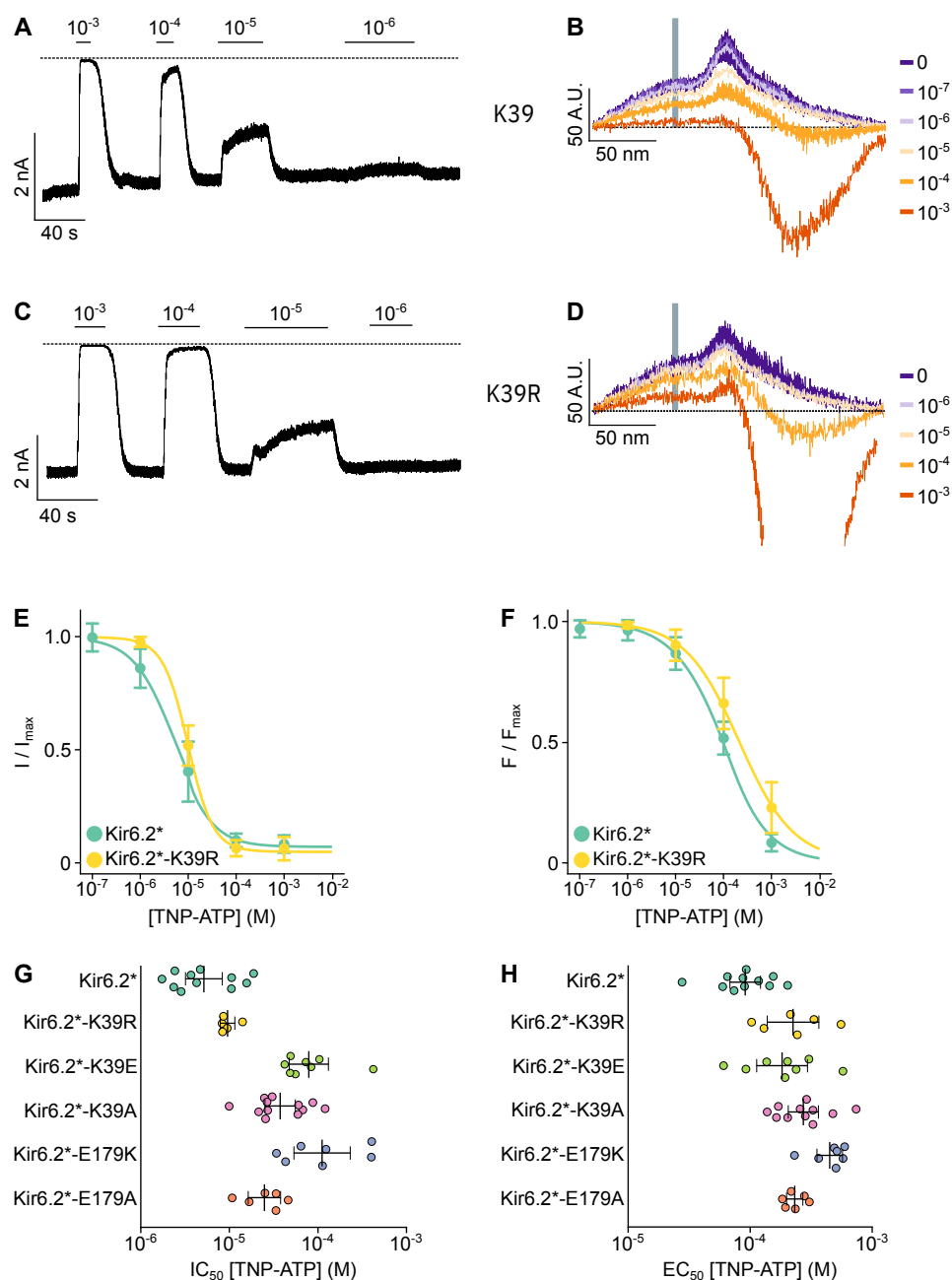
Figure 5

Figure 5. Effect of TNP-ATP on K_{ATP} current. A, B) Representative current (A) and fluorescence (B) traces for Kir6.2*. A) Top solid bars indicate application of TNP-ATP, with concentrations given in M. Dashed line indicates the zero-current level. B) The grey bar indicates the fluorescence peak corresponding to ANAP. The colours indicate application of TNP-ATP, with concentrations given in M. The dashed line indicates the zero-fluorescence level with respect to background. C, D) Representative current (C) and fluorescence (D) traces for Kir6.2*-K39R . E, F) Concentration-response relationships for TNP-ATP current inhibition (C, I/I_{max}) and fluorescence quenching (D, F/F_{max}) of Kir6.2* (Kir6.2*, green) and Kir6.2*-K39R (Kir6.2*-K39R, yellow). Data points are the mean and error bars are the 95% confidence intervals. Smooth lines are fits to the Hill equation, with coefficients given in figure 5, table supplement 1. G, H) IC_{50}s from TNP-ATP current inhibition (G) and EC_{50}s from TNP-ATP fluorescence quenching (H) derived from Hill fits to individual experiments are plotted as coloured data points. The means and 95% confidence intervals for each construct are overlaid as black error bars. Each construct is labelled with GFP at the C-terminus, ANAP at residue W311 and co-expressed with SUR1.
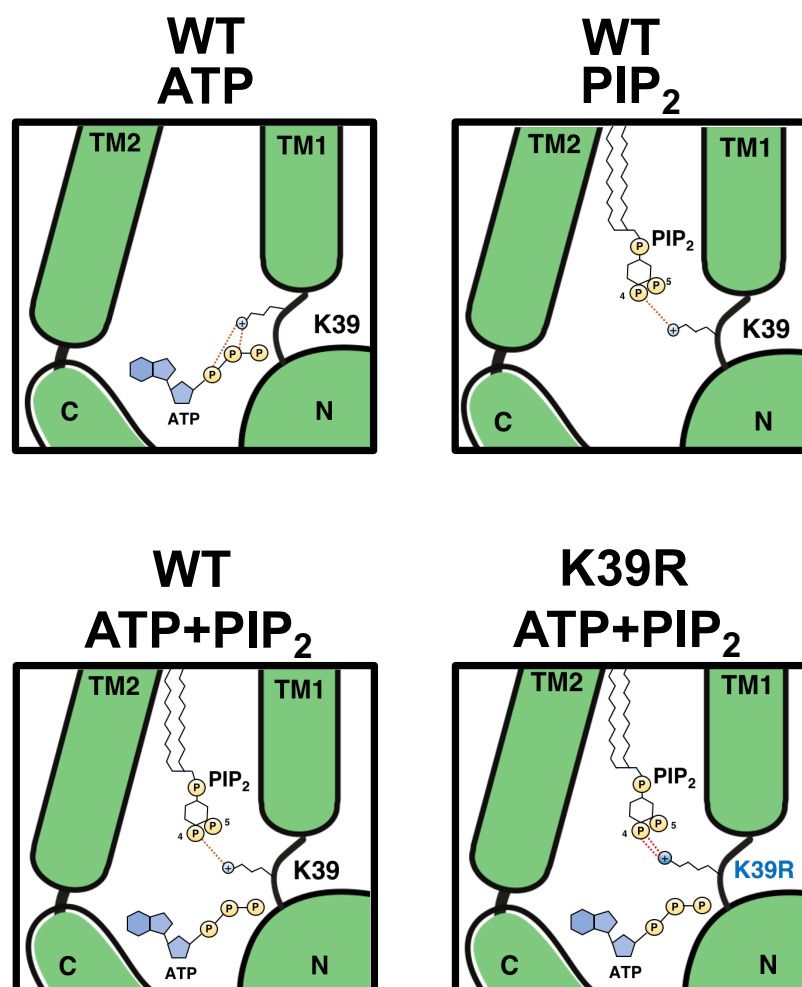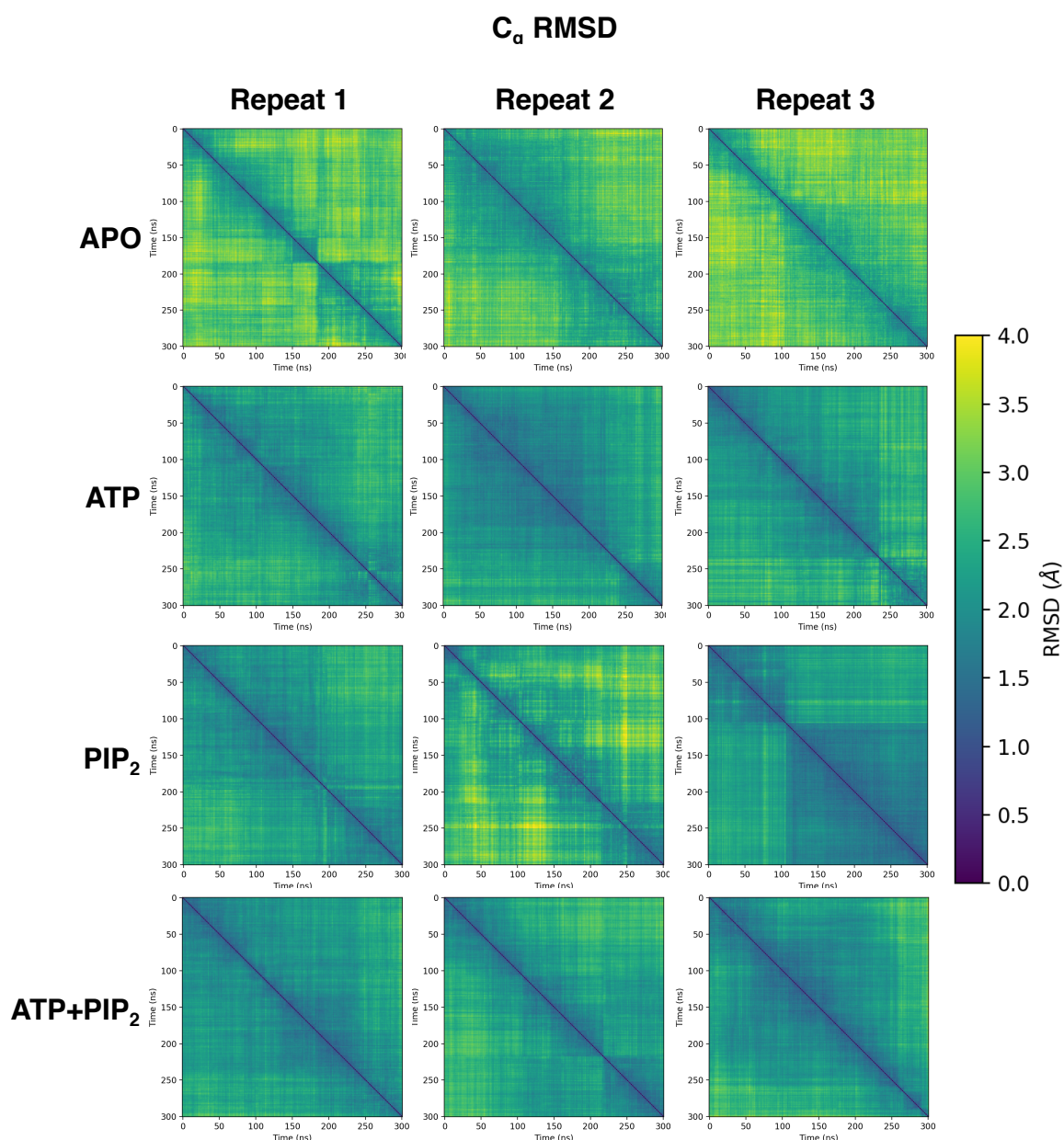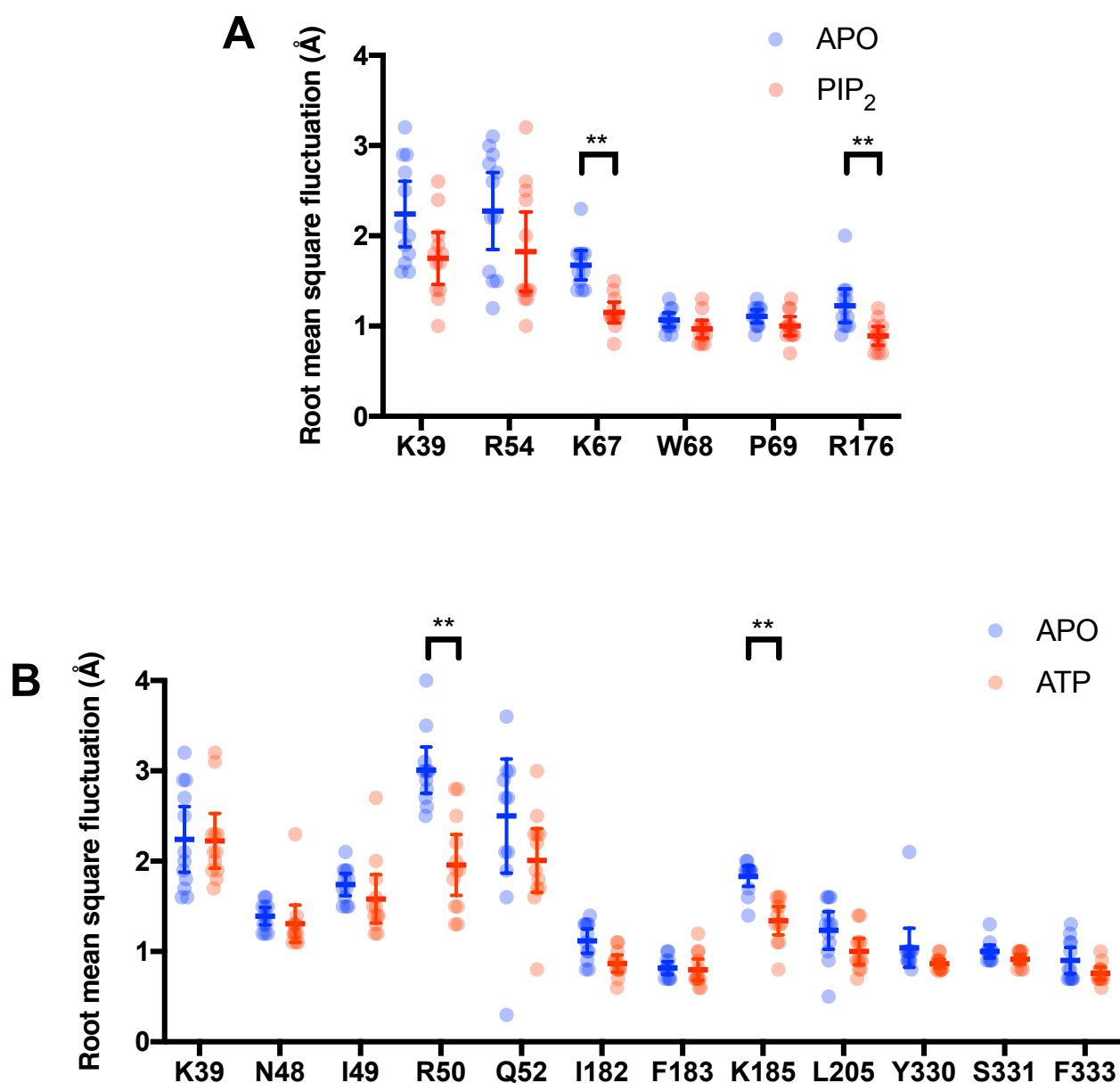
Figure 6

Figure 6. Schematic representation of the interaction between Kir6.2, ATP and PIP$_2$. Interaction between ATP (silver sphere), PIP$_2$ (hexagon with silver phosphate group – P) and Kir6.2 (green). A positive charge on K39 is denoted in yellow (or red in the K39R mutant). The orange dashed line represents hydrogen bonds between K39 and the ligand.
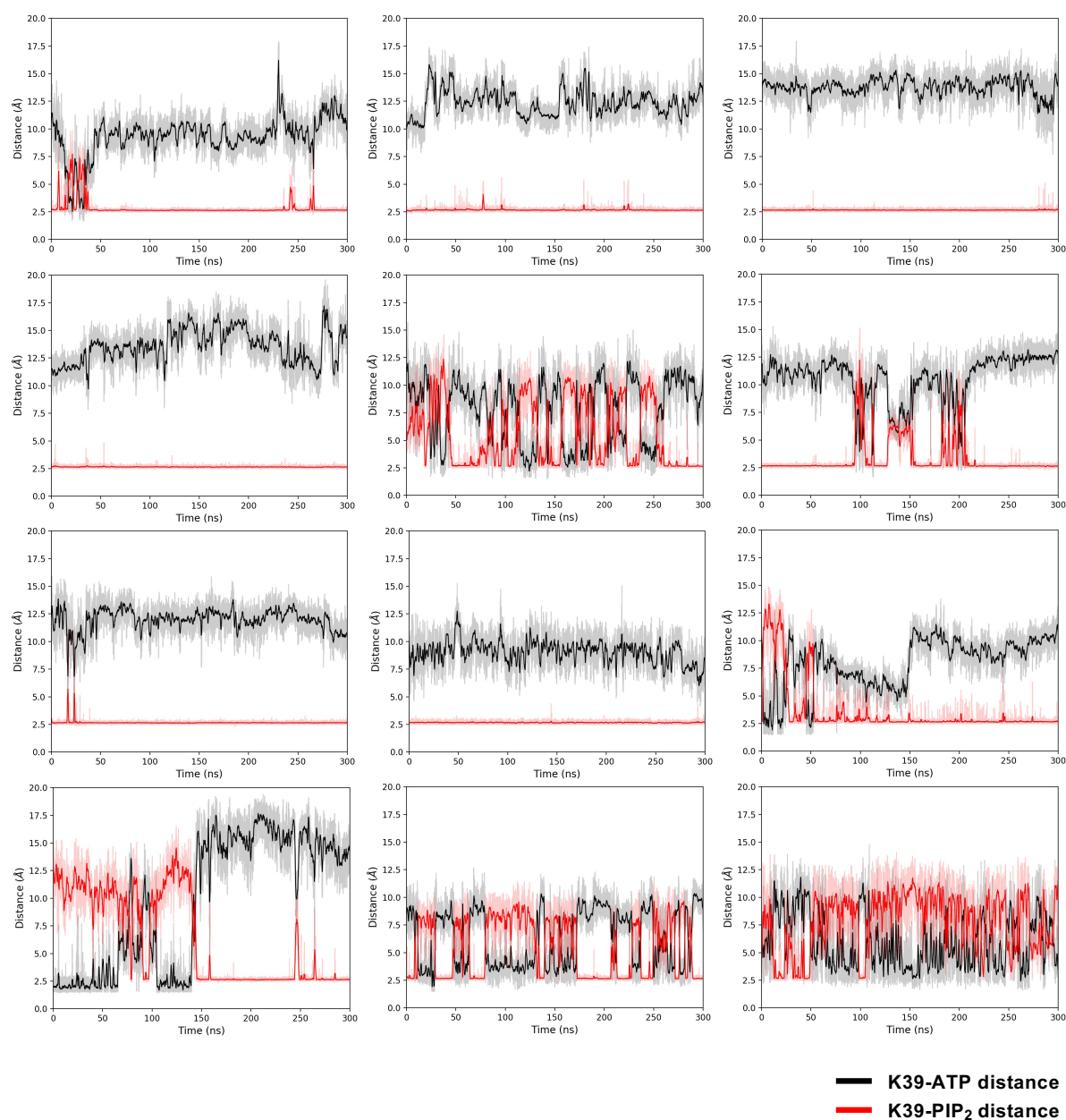
Supplementary figure 1

Supplementary figure 1. Overall protein dynamics in different states of the simulation. Pairwise Root Mean Square Deviation (RMSD) analysis of the C_α atoms of Kir6.2 in the different ligand-bound states, measured over the final 300 ns simulation trajectory (n=3). The colorbar indicates the RMSD value ranging from 0 to 4 Å.
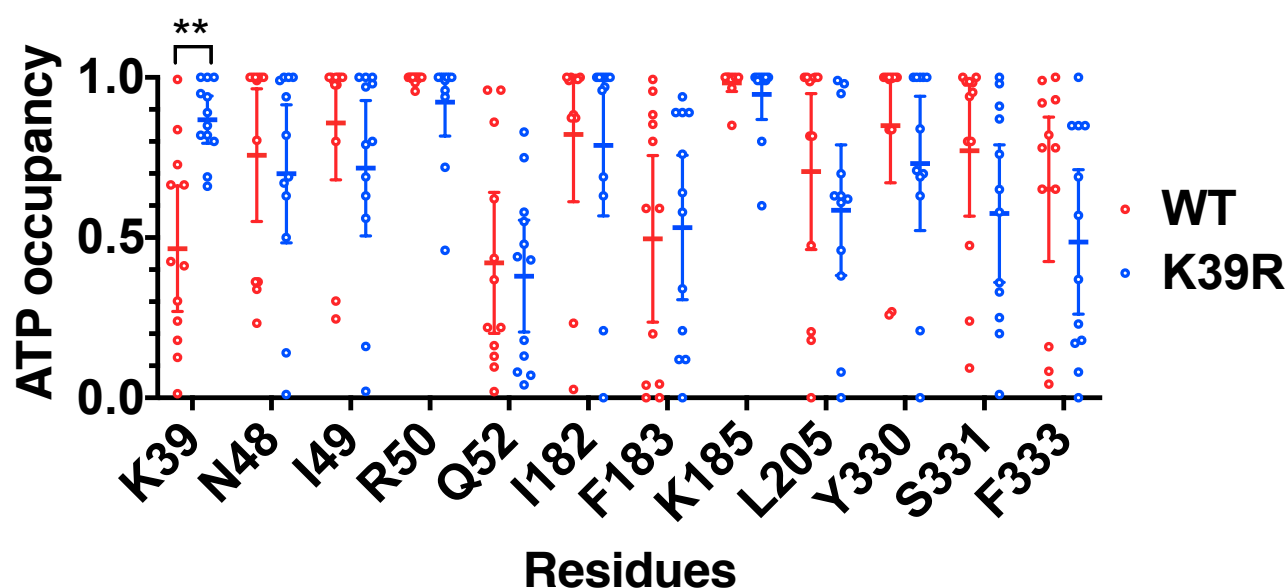
Supplementary figure 2

Supplementary figure 2. The dynamics of individual side chains in the simulation. A) Root mean square fluctuation (RMSF) analysis of the residues on the Kir6.2 tetramer which made contact with the PIP_2 molecule in the absence (blue) and the presence (red) of PIP_2 (n = 12). The error bar indicates the 95% confidence interval around the mean. ** $p < 0.01$ (Student's t-test). B) Root mean square fluctuation (RMSF) analysis of the residues on the Kir6.2 tetramer which made contact with the ATP molecule in the absence (blue) and the presence (red) of ATP (n = 12). The error bar indicates the 95% confidence interval around the mean. ** $p < 0.01$ (Student's t-test).
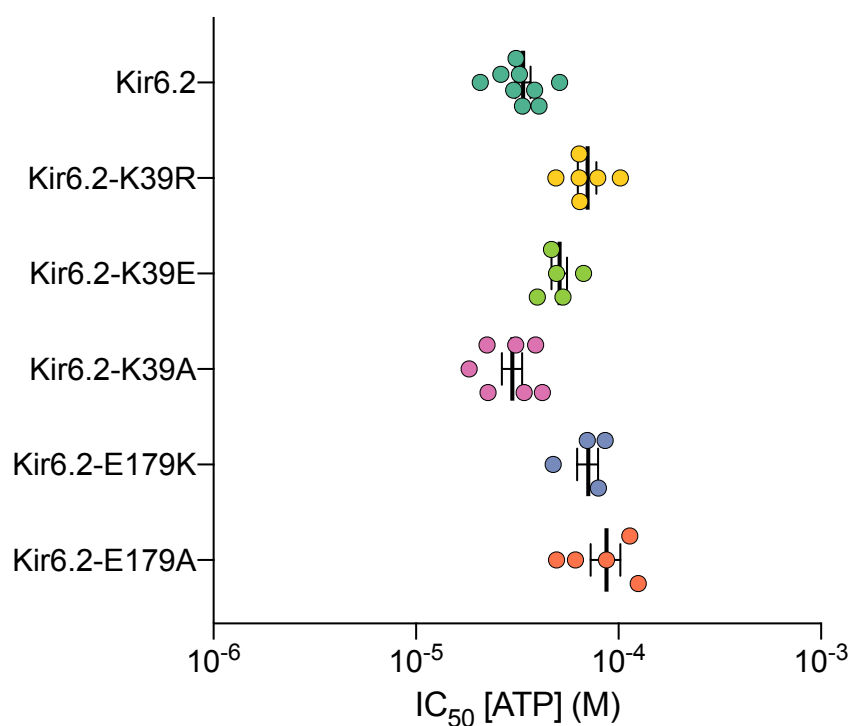
Supplementary figure 3

Supplementary figure 3.. The distance between K39, ATP and PIP$_2$. Distance calculation of the ATP (black) and PIP$_2$ (red) and the K39 when both ligands are present, measured over the final 300 ns simulation trajectory. The darker lines show running averages of every 1 ns of the simulation.
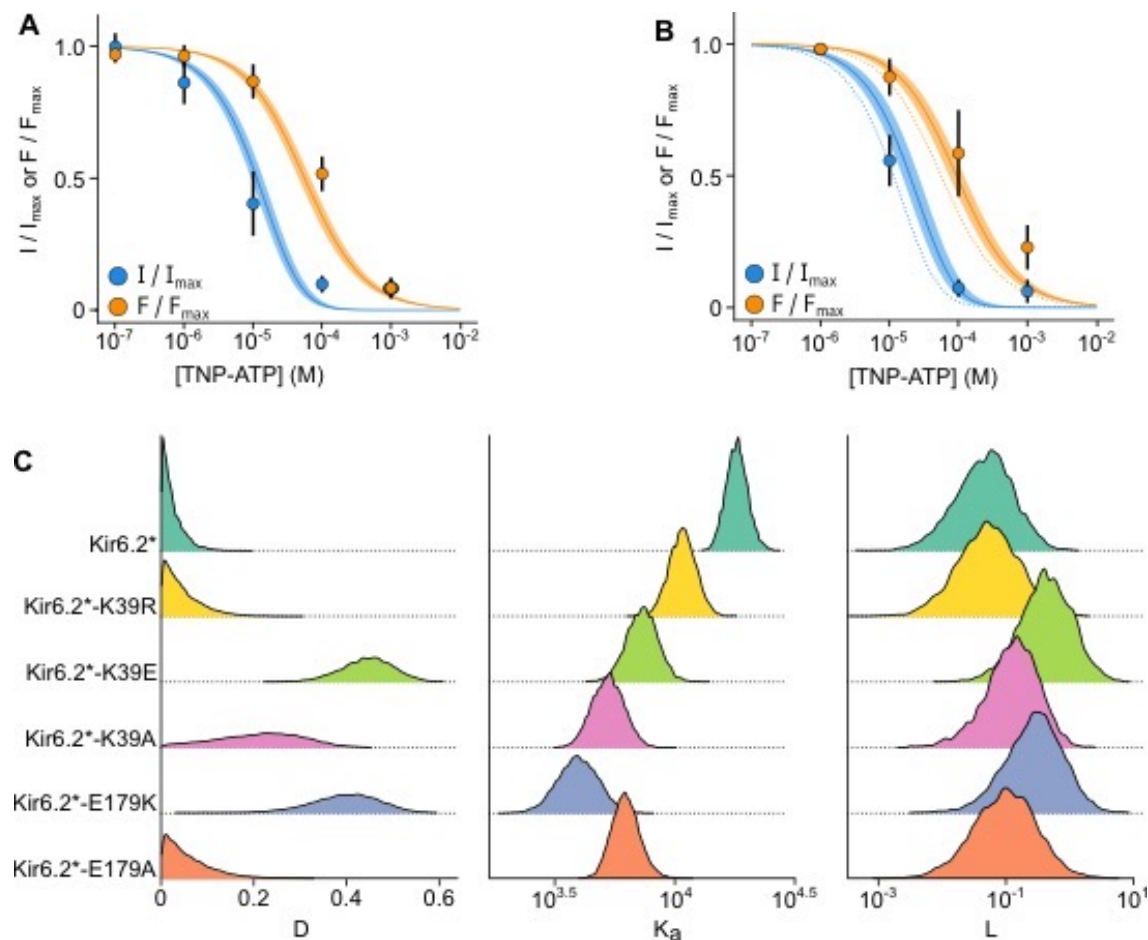
Supplementary figure 4

Supplementary figure 4. An effect of ATP occupancy caused by K39R mutation. ATP contact analysis showing the fraction of time that residues which contact the ATP molecule >40% in all 12 repeats of 300 ns simulations are within 4 Å proximity to the channel (ATP occupancy) for WT (red) and the K39R mutant (blue). The error bar indicates the 95% confidence interval around the mean. ** $p < 0.01$ (Student's t-test).

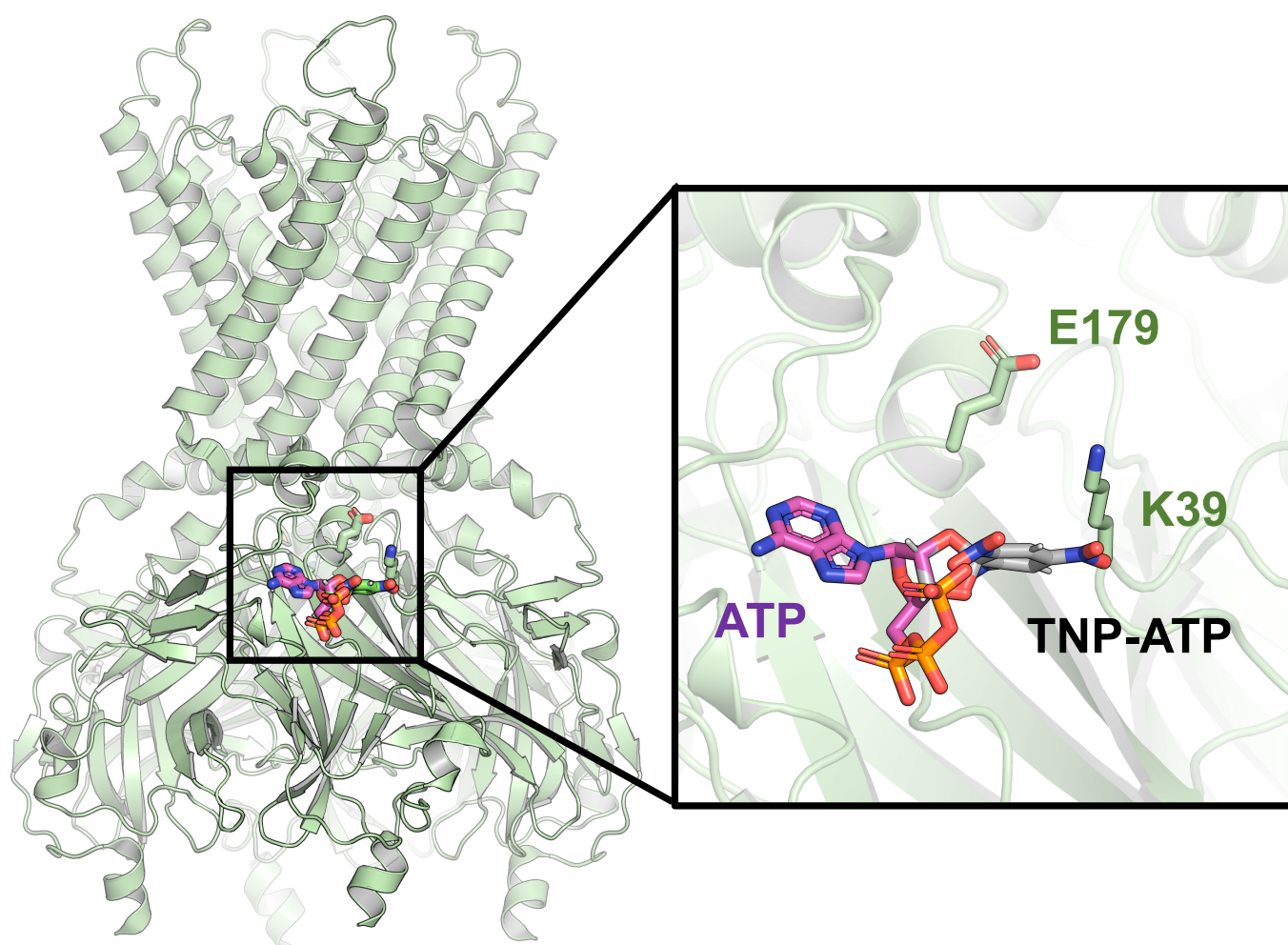# Supplementary figure 5

Supplementary figure 5. Effect of ATP on K_{ATP} current. IC_{50}s from ATP current inhibition derived from Hill fits to individual experiments are plotted as coloured data points. The means and 95% confidence intervals for each construct are overlaid as black error bars. Each construct is labelled with GFP at the C-terminus, but not with ANAP at residue W311.

Supplementary figure 6

Supplementary figure 6. MWC-type modelling A, B) Concentration-response relationships for TNP-ATP inhibition of currents (I/I_{max}) and for quenching of ANAP fluorescence (F/F_{max}) for Kir6.2* (A) or Kir6.2*-K39R (B). Data points are the mean and error bars are the 95% confidence intervals. Data were fit to an MWC-type model. Solid curves represent the median fits and shaded areas indicate the 95% quantile intervals. B) The median fits to Kir6.2* in panel A are shown here as dotted lines. C) Posterior probability distributions for the MWC-type model parameters for each construct.

Supplementary figure 7

Supplementary figure 7. Alignment of TNP-ATP and ATP on the Kir6.2 structure. Alignment of TNP-ATP to ATP on the Kir6.2 structure. TNP-ATP is represented in grey, ATP in purple. K39 and E179 side chains are represented as stick in green.

Supplementary table 1

Construct	IC$_{50}$ (µM) [ATP]	Dunnett's adjusted p-value
Kir6.2	34±3 (9)	Control
Kir6.2-K39A	31±4 (7)	0.95
Kir6.2-K39E	61±7 (5)	<0.01
Kir6.2-K39R	74±7 (6)	<0.01
Kir6.2-E179A	90±12 (5)	<0.01
Kir6.2-E179K	82±8 (4)	<0.01

Supplementary table 1. IC$_{50}$s from ATP current inhibition of Kir6.2 with SUR1. Each construct is labelled with GFP at the C-terminus, but not with ANAP at residue W311. The number of repeats per construct is shown in parenthesis. The error shows standard error of the mean. h = 1.3-1.7 for fits to the concentration-response relationships for ATP inhibition. p-values are calculated using Dunnet's post-hoc test in comparison to control (Kir6.2) after a one-way ANOVA.

Supplementary table 2

Construct	IC$_{50}$ (µM) [ATP]	Dunnett's adjusted p-value
Kir6.2*	112±9 (8)	Control
Kir6.2*-K39A	169±21 (8)	0.15
Kir6.2*-K39E	173±22 (6)	0.038
Kir6.2*-K39R	445±33 (8)	<0.01
Kir6.2*-E179A	376±80 (5)	<0.01
Kir6.2*-E179K	351±63 (8)	<0.01

Supplementary table 2. IC$_{50}$s from ATP current inhibition of Kir6.2* with SUR1. Each construct is labelled with GFP at the C-terminus, and ANAP labelled at residue W311. The number of repeats per construct is shown in parenthesis. The error shows standard error of the mean. h = 1.3-1.7 for fits to the concentration-response relationships for ATP inhibition. p-values are calculated using Dunnet's post-hoc test in comparison to control (Kir6.2*) after a one-way ANOVA.

Supplementary table 3

Construct	IC$_{50}$ (µM) [ATP]
Kir6.2	208±36 (3)
Kir6.2-K39A	*nd**
Kir6.2-K39E	1280±na (1)
Kir6.2-K39R	384±19 (3)
Kir6.2-E179A	1293±304 (4)
Kir6.2-E179K	378±178 (4)

Supplementary table 3. IC$_{50}$s from ATP current inhibition of Kir6.2 without SUR1. Each construct is labelled with GFP at the C-terminus, but not with ANAP at residue W311. The number of repeats per construct is shown in parenthesis. *nd**, *not determined*, no macroscopic current was measured when mutant was expressed in the absence of SUR1. h = 0.9-1.3 for fits to the concentration-response relationships for ATP inhibition. The error shows standard error of the mean.

Supplementary table 4

Construct	IC_{50} (µM) [TNP-ATP]	Dunnett's adjusted p-value
Kir6.2	1.39±0.40 (12)	Control
Kir6.2-K39A	13.2±0.28 (8)	<0.01
Kir6.2-K39E	12.6±0.44 (5)	<0.01
Kir6.2-K39R	2.62±0.44 (9)	0.054
Kir6.2-E179A	13.6±3.24 (7)	<0.01
Kir6.2-E179K	56.3±17.8 (7)	<0.01

Supplementary table 4. IC_{50}s from TNP-ATP current inhibition of Kir6.2 with SUR1. Each construct is labelled with GFP at the C-terminus, but not with ANAP at residue W311. Brackets show number of repeats per construct. The error shows standard error of the mean. h = 1.3-1.7 for Hill fits to the concentration-response relationships of individual experiments for TNP-ATP inhibition p-values are calculated using Dunnet's post-hoc test in comparison to control (Kir6.2) after a one-way ANOVA.

Supplementary table 5

	IC_{50} (µM) [TNP-ATP]	Dunnett's adjusted p-value
Kir6.2*	7.06±1.79 (11)	Control
Kir6.2*-K39A	46.8±9.48 (12)	<0.01
Kir6.2*-K39E	110±45.2 (8)	<0.01
Kir6.2*-K39R	9.81±0.90 (6)	0.44
Kir6.2*-E179A	27.7±5.23 (6)	<0.01
Kir6.2*-E179K	169±61.7 (7)	<0.01

Supplementary table 5. IC_{50}s from TNP-ATP current inhibition of Kir6.2* with SUR1. Each construct is labelled with GFP at the C-terminus, but with ANAP labelled at residue W311. Brackets show number of repeats per construct. The error shows standard error of the mean. h= 0.9-1.3 for Hill fits to the concentration-response relationships of individual experiments of TNP-ATP inhibition p-values are calculated using Dunnet's post-hoc test in comparison to control (Kir6.2*) after a one-way ANOVA.

Supplementary table 6

	EC$_{50}$ (µM) [TNP-ATP]	Dunnett's adjusted p-value
Kir6.2*	94.4±14.0 (11)	Control
Kir6.2*-K39A	244±61.4 (11)	<0.01
Kir6.2*-K39E	165±60.1 (8)	0.02
Kir6.2*-K39R	209±72.7 (6)	<0.01
Kir6.2*-E179A	170±23.6 (6)	<0.01
Kir6.2*-E179K	171±60.5 (7)	<0.01

Supplementary table 6. EC$_{50}$s from TNP-ATP FRET of Kir6.2* with SUR1. Each construct is labelled with GFP at the C-terminus, but with ANAP labelled at residue W311. Brackets show number of repeats per construct. The error shows standard error of the mean. h = 0.9-1.3 for Hill fits to the concentration-response relationships of individual experiments of TNP-ATP inhibition. p-values are calculated using Dunnet's post-hoc test in comparison to control (Kir6.2*) after a one-way ANOVA.